



**Photo-assisted electrodeposition of MoS_x from ionic liquid
on organic-functionalized silicon photoelectrodes for H₂
generation**

Journal:	<i>Journal of Materials Chemistry A</i>
Manuscript ID	TA-ART-11-2015-009684.R1
Article Type:	Paper
Date Submitted by the Author:	24-Feb-2016
Complete List of Authors:	Redman, Daniel; The University of Texas at Austin, Department of Chemistry Kim, Hark Jin; The University of Texas at Austin, Chemistry Stevenson, Keith J.; The University of Texas at Austin, Department of Chemistry; Skolkovo Institute of Science and Technology Rose, Michael; The University of Texas at Austin,



ARTICLE

Photo-assisted electrodeposition of MoS_x from ionic liquid on organic-functionalized silicon photoelectrodes for H₂ generation

Received 00th January 20xx,
Accepted 00th January 20xx

DOI: 10.1039/x0xx00000x

www.rsc.org/

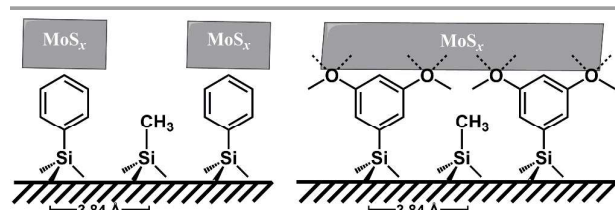
Daniel W. Redman^{a,†}, Hark Jin Kim^{a,†}, Keith J. Stevenson^{a,b,*} and Michael J. Rose^{a,*}

This work reports on the synergistic utility of ionic liquid-based, photo-assisted electrodeposition of MoS_x onto organic-functionalized silicon photoelectrodes for dihydrogen (H₂) evolution under 1-sun illumination. The surface linker 3,5-dimethoxyphenyl covalently attached to Si(111) enhances conductivity at the substrate|electrolyte interface (impedance spectroscopy) and provides improved physico-chemical support for MoS_x deposition (SEM, Raman, PEC-deposition, XPS), to generate a functional composite device that results in 0.33% efficiency for solar→H₂ conversion. We report a new method of ionic liquid-based MoS_x deposition that avoids complications in analogous aqueous procedures, and facilitates the deposition of a uniform catalytic film. This work provides a generalized framework for optimization of non-platinum catalysts for solar→H₂ conversion.

Introduction

There have been a considerable number of reports in the field of solar fuels using silicon photoelectrodes with surface functionalization – such as organics, microwires, nanowires,^{1–3} metal oxides (SiO₂, Al₂O₃, TiO₂)^{4–6} and metal nanoparticles (Pt, Ni, Ni-Mo, Au)^{7–10} – all to enhance photocatalytic activity. Silicon as a light-absorber is an attractive material due to its low cost and high earth abundance. One method used to enhance the electrochemical performance of silicon photoelectrodes is the modulation of energy barrier heights by surface modification using organic molecules. In the past decade, Lewis and co-workers have reported intriguing results demonstrating that different organic-modified Si(111) surfaces show different electrochemical performance, induced either by changes in the barrier height, surface dipole, or synergistic modulation of both. For example, H-terminated *p*-Si(111) showed a higher *V*_{OC} by 300 mV than CH₃-terminated *p*-Si(111) surface in acetonitrile solution containing diacetylcobaltocene.¹¹ In related work, we recently reported that the band edge modulation of a *p*-Si photocathode by surface functionalization with aromatic moieties, such as methyl, phenyl (Ph), naphthyl, anthryl, and 3,5-dimethoxyphenyl (diOMe).¹² In particular, 3,5-dimethoxyphenyl-terminated Si substrate exhibited a high *p*-

type energy barrier height (high *V*_{OC}), as well as a low series resistance due to its chemical (*vis-à-vis* electronic) connectivity with a TiO₂ thin film supporting platinum (Pt) nanoparticles as catalyst for hydrogen (H₂) evolution. The relatively low series resistance of 3,5-dimethoxyphenyl surface was postulated to emanate from an enhanced interaction between bulk Si and the coordinative TiO₂ layer via the oxygen moieties of –OCH₃ functional groups.^{13–16} However, the prohibitive cost of Pt could prevent its widespread and low-cost application in solar fuels devices.



Scheme 1: Schematic representation of the *p*-Si(111)|R|MoS_x catalyst constructs utilized in this work (R = CH₃, Ph, 3,5-dimethoxybenzene).

The earth abundant catalyst molybdenum disulfide, MoS₂, has attracted great attention as an alternative catalyst for the hydrogen evolution reaction (HER), showing promise as a substitute for Pt. For example, Chorkendorff et al. reported results for molybdenum sulfide catalyst on metal passivated *n*⁺*p*-Si photocathode; both a MoS_x/MoS₂/*n*⁺*p*-Si heterostructure prepared by sputtering/sulfurization, and MoS_x/Ti/*n*⁺*p*-Si photoelectrode prepared by electrodeposition exhibited an onset potential of 0.33 V vs. RHE in 0.1 M HClO₄ solution.^{17,18} In related work, drop-cast Mo₃S₄ clusters on H-terminated Si(111) planar electrode displayed a shift in onset potential from -0.4 V to +0.15 V (vs. RHE) with 8 mA cm⁻² of current density at 0 V (vs. RHE).¹⁹ In two other cases, the research groups of Loo and Yang independently reported the

^a Department of Chemistry, The University of Texas at Austin, Austin, TX, 78712, United States

^b Skoltech Center for Electrochemical Energy Storage, Skolkovo Institute of Science and Technology, Moscow 143026, Russia

* corresponding authors: k.stevenson@skoltech.ru, mrose@cm.utexas.edu

† Denotes equal authorship.

Electronic Supplementary Information (ESI) available: Contains additional figures cited in the text See DOI: 10.1039/x0xx00000x

ARTICLE

Journal of Materials Chemistry A

integration of MoS₂ with silicon nanowire electrodes: an onset potential of +0.25 V (vs. RHE) for SiNW@MoS₂ in 1.0 M Na₂SO₄ buffer (pH 5.0); and +0.3 V (vs. RHE) for MoS₂/TiO₂/n⁺p-Si NW in 0.5 M H₂SO₄.^{20,21} Furthermore, Jin et al. investigated the catalytic activity of Si|MoS₂ with different crystal structures, based on preparation by different deposition methods.²² The as-grown MoS₂ (2H-MoS₂) prepared by chemical vapor deposition was converted to metallic MoS₂ (1T-MoS₂) by chemical exfoliation with *n*-BuLi. CVD 1T-MoS₂ showed a positive onset potential (+0.25 V vs. RHE), effected by a dramatic decrease in charge transfer of the catalytic reaction ($R_{ct_CVD\ 1T} = 49.2\ \Omega\text{-cm}^2$) compared to CVD 2H-MoS₂ (+0.23 V, $R_{ct_CVD\ 2H} = 992.6\ \Omega\text{-cm}^2$) and drop-casted 1T-MoS₂ (+0.23 V, $R_{ct_DC\ 1T} = 212.4\ \Omega\text{-cm}^2$). Jin and co-workers also examined the catalytic activity of amorphous MoS_xCl_y *p*-Si and found +0.27 V (vs. RHE) shift in the onset potential.²³ When this same material was interfaced with n⁺p-Si micropylramids +0.41 V (vs. RHE) shift in the onset potential was observed.²⁴ And although MoS₂ seems to fit the requirement of HER catalyst, the deposition method such as sputtering, sulfurization, and CVD each present limitations of economy, safety and performance.

Electrodeposition offers an efficient, low cost, and scalable method to prepare thin films. It has been reported by several groups that the [MoS₄]²⁻ ion serves as a precursor for the electrodeposition of amorphous MoS_x ($x = 2-3$).²⁵⁻²⁷ The stoichiometry of the films can be controlled by the electrodeposition procedure; anodic deposition leads to the formation of MoS₃, while cathodic deposition leads to the formation of MoS₂. Merki and Vrabel et al. have shown that MoS_x deposited anodically, cathodically, and by cycling between the two regimes showed high activity for HER.^{27,28} Much work to date has been performed in aqueous solutions, with the exception of two studies where MoS₂ was electrodeposited in ethylene glycol.^{29,30} The presence of water in the deposition bath can lead to undesired oxidation of the substrate – or the deposited catalyst – thus leading to degradation in performance. Our group has shown that ionic liquids are promising alternative electrolytes for the electrodeposition of reactive metals and compounds that cannot typically be deposited in aqueous electrolytes, due to their large electrochemical windows, low volatility, and absence of water and reactive oxygen species.³¹⁻³³

Electrodeposition on semiconductor surfaces can be enhanced by exposure to light. On *p*-type semiconductors light promotes an electron to the conduction band or a surface state that can then reduce a species in solution. Notably, light can also be used to control different aspects of the deposition. Kawamura et al. have shown that light can be used to control size and particle density for metals such as Co, Ni, and Cu.³⁴ In the case of Pt electrodeposition, the intensity of light has a similar effect to potential: higher intensity leads to small particles with a high particle density, while low light intensity leads to larger particles with a low particle density.³⁵ Platinum films on *p*-Si prepared by photo-assisted electrodeposition have been shown to outperform films prepared by electrodeposition in the dark, e-beam evaporation, or sputter deposition.^{36,37}

Overall, in this work our aims were thus three-fold: (i) to characterize the electrochemical properties of the dimethoxyphenyl surface, (ii) to investigate its role in promoting or stabilizing MoS_x films during electrodeposition in ionic liquids, and (iii) to synergistically optimize the organic and inorganic components to maximize PEC performance for H₂ evolution. We have utilized surface characterization (contact angle, XPS, Raman) and electrochemical techniques (electrodeposition, spectroelectrochemistry, impedance spectroscopy, linear sweep voltammetry) to achieve these aims.

Results and discussion

Surface Characterization

Table 1. Water Contact Angle and Surface Coverage for Organic-Terminated *p*-Si(111) Surfaces

Surfaces	Water Contact Angle, θ^{water} (°)	XPS Intensity ^d		Surface Coverage (%) ^e
		C 1s (C-Si)	C 1s (sp ²)	
<i>p</i> -Si(111) diOMe	55.4 ± 1.4	0.2073	0.2340	46.80
<i>p</i> -Si(111) Ph	64.1 ± 2.1	0.1872 ^c	0.2753 ^c	55.06 ^c
<i>p</i> -Si(111) OH	56.2 ± 1.7 ^d			
<i>p</i> -Si(111) CH ₃	110.8 ± 0.8 ^d			

^aRelative intensity to the Si 2p (Si-C bonded). ^bRelative coverage of concerned molecule to the ideal value of 0.5. ^cValue from ref 12. ^dValue from ref 39.

We hypothesized that the higher charge density at the oxygen-containing surface moiety (3,5-dimethoxyphenyl) would afford enhanced electrodeposition performance in ionic liquid media due to improved conductance at the substrate|electrolyte interface. To investigate this hypothesis, we first evaluated the surface hydrophilicities of *p*-Si(111)|Ph and *p*-Si(111)|diOMe substrate by measuring the water contact angle (θ^{water}), a common indicator of surface hydrophilicity. As shown in Table 1, the *p*-Si(111)|diOMe surface exhibits a contact angle of 55.4 ± 1.4°, consistent with our previous report.³⁸ This value is similar to that observed for the super-hydrophilic (100% OH-terminated) substrate (56.2 ± 1.7°), and quite distinct from the super-hydrophobic (100% CH₃-terminated) surface (110.8 ± 0.8°). This result indicates that the *p*-Si(111)|diOMe surface has a strong hydrophilic nature that is comparable to the super-hydrophilic OH-terminated surface. On the other hand, the hydrocarbon-only substrate *p*-Si(111)|Ph surface shows a modest increase in the contact angle (64.1 ± 2.1°), due to the absence of any oxygen group on the organic moiety. To ensure this observed difference was caused only by the identity of the organic species, their respective surface coverages were evaluated via X-ray photoelectron spectroscopy by the comparison of I_{C-1s}/I_{Si-2p} ratio via. The assigned Si 2p and C 1s spectra for the *p*-Si(111)|diOMe and *p*-Si(111)|Ph are available in Supporting Information (Figure S2) and Ref 15, respectively. From the literature,¹⁴ we accepted that the theoretical maximum value of I_{C-1s}/I_{Si-2p} for ~100% covered alkyl monolayer (e.g. methyl) is ~0.5. However, the quantification of

I_{C-Si}/I_{Si-C} (caused by $-CH_3$) portion of the p -Si(111)|diOMe substrate is ~ 0.21 , which is roughly half of the theoretical maximum value. The remnant value can be obtained by the sp^2 component derived from the aromatic species. The calculated coverage of sp^2 carbon on p -Si(111)|diOMe is ~ 0.23 , which is in agreement with p -Si(111)|Ph substrate (~ 0.28). Moreover, the sum of the surface coverage of p -Si(111)|diOMe (44%), quantified by C_{C-Si} and C_{sp^2} , is consistent with the benchmark value of phenyl coverage reported by established researchers (52%) and our analogous report (45%).^{14,39} This result indicates that (i) the 3,5-dimethoxyphenyl is effectively bonded on Si atom sites, and (ii) the surface coverage is nearly identical to the p -Si(111)|Ph substrate. Thus, the hydrophilicity of the surface is likely caused by the H-bonding lone pair on the methoxy groups ($-OCH_3$), and possibly its enhanced dipole.

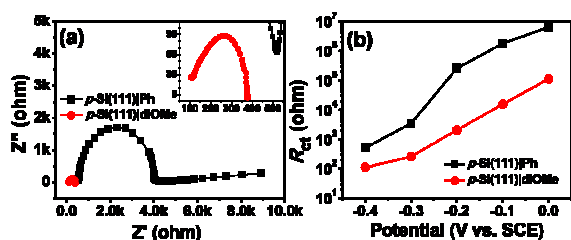


Figure 1: (a) Nyquist plots for p -Si(111)|Ph (black) and p -Si(111)|diOMe (red) substrates. The inset is a magnification of the p -Si(111)|diOMe Nyquist plot. (b) Potential dependence of the charge transfer resistance as determined by EIS. Solution 0.5 M $H_2SO_4(aq)$, 1-sun irradiation, 10 mV AC amplitude, frequency range $10^5 < f < 0.1$ Hz.

We next hypothesized that the hydrophilicity and the increased charge density from the oxygen moieties would enhance the charge transfer reaction between the electrode surface and the electrolyte. To test this, electrochemical impedance spectroscopy (EIS) was employed. EIS measurements were performed with a frequency range of 10^5 – 0.1 Hz under 1-sun irradiation with various applied potentials. The obtained Nyquist plots with -0.3 V vs. SCE for p -Si(111)|diOMe and p -Si(111)|Ph substrate are shown in Figure 1a. The x-intercept of high frequency (low x-axis) and the diameter of the semicircle correspond to the uncompensated resistance (R_s) and the charge transfer resistance (R_{ct}), respectively. From the fitting with Randle's equivalent circuit [$R(CPE,R)$, R : resistance element, CPE : constant phase element – non-ideal capacitance], the R_{ct} of p -Si(111)|Ph is $3.47 \times 10^3 \Omega$, while that of p -Si(111)|diOMe surface is $2.66 \times 10^2 \Omega$. This remarkable decrease in resistance on the diOMePh surface (~ 10 fold) of R_{ct} was observed in all experiments (applied potentials between -0.4 and 0 V vs. SCE), as shown in Figure 1b. Furthermore, the same trend of lower R_{ct} of p -Si(111)|diOMe than p -Si(111)|Ph surface was also found in non-aqueous solution (Figure S3 in SI). Lastly, the same experiment on a super-hydrophobic p -Si(111)| CH_3 substrate (Figure S3c and d, 0.5 M H_2SO_4) afforded a charge transfer resistance of $1.33 \times 10^5 \Omega$. From these results, it is evident that the hydrophilic nature of the surface and the increased charge density resulting from the oxygen moieties accelerates the charge transfer rate at the electrode|electrolyte interface.

Therefore, out of the three EIS-tested electrodes, the p -Si(111)|diOMe substrate was pursued as the most promising substrate for the photo-assisted electrodeposition of the catalyst.

Photo-Assisted Electrodeposition of MoS_x

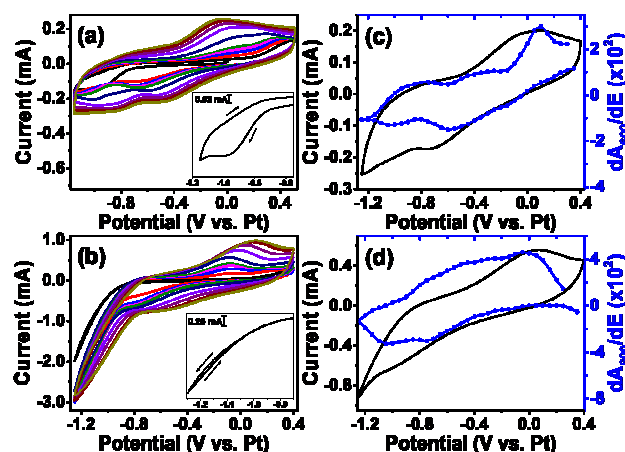
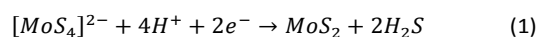
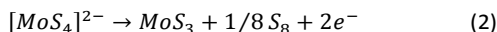


Figure 2: CV deposition of MoS_x on glassy carbon electrodes from 0.005 M $[MePipH]_2[MoS_4]$ in EMIM-TFSI in the (a) absence and (b) presence of 0.2 M $[PipH][TFSI]$, scans 1-5, 10, 20, 30, 40, 50. Inset of (a) and (b) show the first scan of the depositions. 25th scan of cyclic voltammogram and corresponding derivative cyclic voltabsorptogram of 0.005 M $[MePipH]_2[MoS_4]$ on an FTO electrode in the (c) absence and (d) presence of 0.2 M $[PipH][TFSI]$, $\lambda = 600$ nm, Scan Rate = 50 mV/s.

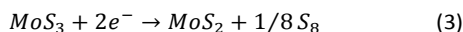
The electrochemistry of $[MePipH]_2[MoS_4]$ in EMIM-TFSI was first investigated on glassy carbon electrodes using cyclic voltammetry in the absence (Figure 2a) and the presence (Figure 2b) of 0.2 M $[PipH][TFSI]$ (a proton donor). In both cases, cycling the $[MoS_4]^{2-}$ precursor between $+0.5$ and -1.25 V vs. Pt leads to a progressive increase in current and the appearance of new features; this behaviour is similar to others' observations in aqueous electrolyte.^{27,28} In the absence of $[PipH][TFSI]$ an anodic peak appears at ca. -0.07 V vs. Pt and two cathodic peaks appear at ca. -0.45 and -0.85 V. In the presence of $[PipH][TFSI]$ an anodic peak appears at ca. $+0.1$ V vs. Pt and one cathodic feature at ca. -0.55 V. When the potential is scanned negative of -0.8 V vs. Pt a large increase in the current is observed, which is likely in part due to the reduction of protons from $[PipH][TFSI]$. In the first scan of $[MoS_4]^{2-}$ in the presence of $[PipH][TFSI]$ (inset of Figure 2b) a nucleation loop is observed, which is absent from the first scan in only EMIM-TFSI (no proton source). This suggests that cathodic deposition only occurs to a significant extent in the presence of excess protons, which has been found to be the case in other aprotic media.²⁹

Two electrochemical reactions have been proposed for the electrodeposition of MoS_x ($x = 2$ or 3) from the $[MoS_4]^{2-}$ ion.^{25,26}





Using UV/vis spectroelectrochemistry we further investigated the differences between the absence or presence of excess protons (via [PipH][TFSI]) on the electrodeposition mechanism of [MePipH]₂[MoS₄]; FTO was used as a transparent working electrode as a model system for these experiments to study the details of the electrodeposition mechanism (for eventual application to Si photodeposition). In Figures 2c and d the 25th scan of the CV deposition of [MePipH]₂[MoS₄] in the absence and presence of [PipH][TFSI], respectively, is plotted alongside the corresponding derivative cyclic voltabsorptogram (DCVA) at 600 nm. In both cases, cathodic scans result in a decrease in dA₆₀₀/dE that results in a peak at ca. -0.6 V or -0.75 V vs. Pt, without and with [PipH][TFSI], respectively. This peak corresponds to a decrease in the concentration of the absorbing species at or near the surface of the electrode, which is attributed to corrosion of the film by the back reaction (Eq 2). Vruble et al. have observed similar results in H₂O using electrochemical quartz crystal microbalance (EQCM).²⁸ As we scan further a second corrosion peak is observed in the DCVA at ca. -1.05 V vs. Pt for both cases. This peak increases as the cycling continues. Based on the findings by Vruble et al., we propose the following reaction accounts for our observations:



The larger increase in dA₆₀₀/dE in the presence of [PipH][TFSI] suggests that the reaction is enhanced by protons. The DCVA of the 25th scan is not a great indicator of whether reaction (1) is occurring; the increase in dA₆₀₀/dE from reaction (1) is drowned out by the decrease in the dA₆₀₀/dE at these potentials from the corrosion reaction and reaction (3). In the first scan in the absence of [PipH][TFSI] (Figure S4a), there is a slight increase in dA₆₀₀/dE between -1.0 and -1.25 V vs. Pt, suggesting reaction (1) may occur to some extent due to the limited availability of protons from the two [MePipH]⁺ counterions of the [MoS₄]²⁻ salt. Alternatively, when an excess of proton source – [PipH][TFSI] – is added, a larger dA₆₀₀/dE response (Figure S4b) is observed between -0.8 and -1.25 V vs. Pt. This supports the claim that protons facilitate reaction (1). As the scan is reversed the dA₆₀₀/dE signal increases to positive values at approximately -1.0 V vs. Pt in both cases. The continuing anodic scan increases the dA₆₀₀/dE signal to features at about +0.1 V and -0.05 V vs. Pt without and with [PipH][TFSI], respectively; this corresponds to the peak in the CV. This result shows that the concentration of the absorbing species at or near the surface of the electrode is increasing, which we attribute to reaction (2).

The electrodeposition of MoS_x on *p*-Si(111)|diOMe and *p*-Si(111)|Ph was performed in the presence of 0.005 M [MePipH]₂[MoS₄], and 0.2 M [PipH][TFSI] was used to facilitate efficient cathodic deposition of MoS_x. When the silicon substrates were exposed to the LED light source, the open circuit potential increased by ca. +0.15 V vs. Pt (Figure S5a and

b), which is similar to the observations of Tran et al.²⁰ Figure 3a shows the effect of light on the current produced by [MoS₄]²⁻ at more negative potentials. The dramatic increase in the current when the substrate is illuminated demonstrates that the Si substrate transfers photo-excited electrons from its conduction band to [MoS₄]²⁻. The MoS_x was electrodeposited by a similar CV deposition scheme, where the potential was cycled between +0.1 and -1.25 V vs. Pt under illumination from the LED source. Potentials more positive than +0.1 V vs. Pt were avoided due to the well-known anodic corrosion of Si substrates (Figure S5c). Figure 3b shows a representative deposition of MoS_x on *p*-Si(111)|diOMe wherein the current increases with each cycle. This is similar to the analogous observations on glassy carbon and FTO substrates. The inset of Figure 3b shows the first scan of the MoS_x deposition where a nucleation loop is present indicating the cathodic deposition of MoS_x. In this potential regime, we expect that the deposition occurs mostly from reaction (1), although it is possible that back reaction (2) also occurs, but to a lesser extent. The electrodeposition of MoS_x on *p*-Si(111)|Ph showed qualitatively similar results to *p*-Si(111)|diOMe (Figure S5d); however quantitatively the current was higher for the *p*-Si(111)|diOMe substrate, thought to be due to the lower charge transfer resistance observed by EIS.

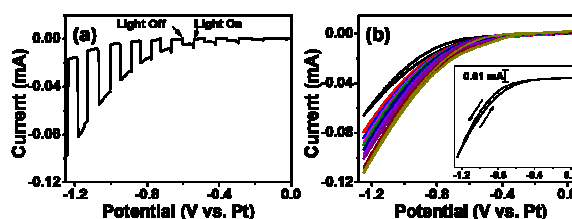


Figure 3: (a) First scan of the CV deposition on *p*-Si(111)|diOMe while alternating light on and off. (b) CV deposition of MoS_x on *p*-Si(111)|diOMe, scans 1-5, 10, 20, 30, 40, 50. Inset: First scans of the CV deposition showing the nucleation loop. Experiment conditions: 0.005 M [MePipH]₂[MoS₄] + 0.2 M [PipH][TFSI] in EMIM-TFSI, 100 W LED irradiation, scan rate = 50 mV/s.

After MoS_x deposition, X-ray photoelectron spectroscopy, Raman spectroscopy and scanning electron microscopy were used to characterize the composition, structure, and morphology of the electrodeposited films on the organic modified *p*-Si substrates. The XPS spectra of the Mo 3*d* region can be fit with two doublets that have Mo 3*d*_{5/2} with binding energies centred at 228.7 and 229.9 eV. The first peak centred at 228.7 eV is attributed to the Mo(IV) ion of MoS_x, and is in agreement with other reports.^{20,27} The second peak at 229.9 eV has been suggested to emanate from a Mo^{z+}O_yS_x species (where *z* = 4 or 5).^{28,40,41} The fit of the S 2*p* region (Figure 4b) shows two doublets with S 2*p*_{3/2} binding energies centred at 161.5 and 163.0 eV, which correspond to S²⁻ and S₂²⁻, respectively.⁴² Considering the total relative areas of the S 2*p* and Mo 3*d*, the S:Mo ratio is ~2.3:1. Analysis of the Mo 3*d* and S 2*p* XPS spectra of *p*-Si(111)|Ph yields similar results (Figure S6c and d). The Raman spectra of *p*-Si(111)|diOMe|MoS_x, *p*-Si(111)|Ph|MoS_x, and GC|MoS_x are presented in the SI Figure S7a-c. The spectrum of *p*-Si(111)|diOMe|MoS_x shows two relatively broad bands

centered at $\sim 310\text{ cm}^{-1}$ and 430 cm^{-1} . These bands have been observed in Raman studies of amorphous MoS_3 , produced by thermal decomposition of $[\text{MoS}_4]^{2-}$, which indicates that the electrodeposited films are amorphous.^{42–44} However, the E_2 mode of silicon at $\sim 520\text{ cm}^{-1}$ prevents the observation of the disulphide (S–S) stretching mode ($510 - 550\text{ cm}^{-1}$) commonly observed for MoS_3 . Relatedly, the Raman spectrum of GC| MoS_x shows a small yet broad band at $\sim 525\text{ cm}^{-1}$, corresponding to the disulphide stretching mode. The relative intensity of the disulphide Raman band to the other bands is unsurprising considering the XPS results show that the S_2^{2-} ions account for only $\sim 19\%$ of the total sulfur content.

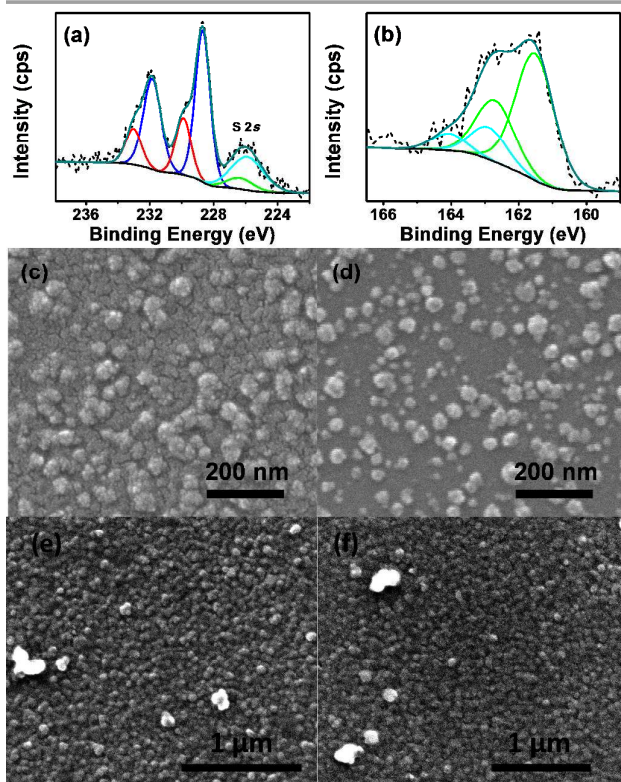


Figure 4: X-ray photoelectron spectra of (a) Mo 3d and (b) S 2p for $p\text{-Si}(111)|\text{diOMe}|\text{MoS}_x$; SEM images for the narrow deposition window ($E = -0.5 - 0.3\text{ V}$ vs. Pt) for (c) $p\text{-Si}(111)|\text{diOMe}|\text{MoS}_x$ and (d) $p\text{-Si}(111)|\text{Ph}|\text{MoS}_x$; SEM images for the full deposition window ($E = -1.25 - 0.1\text{ V}$ vs. Pt) for (e) $p\text{-Si}(111)|\text{diOMe}|\text{MoS}_x$ and (f) $p\text{-Si}(111)|\text{Ph}|\text{MoS}_x$.

Figure 4c,e and d,f depict SEM images of the MoS_x films electrodeposited on $p\text{-Si}(111)|\text{diOMe}$ and $p\text{-Si}(111)|\text{Ph}$ surfaces, respectively. To examine the effects of the organic moieties on the film morphology, a narrow potential window was employed for electrodeposition (between -0.5 to $+0.3$ vs. Pt) (Figure 4c and d). The SEM images highlight the effect of the dimethoxy group on the surface morphology of the MoS_x film deposits on the organic-terminated $p\text{-Si}$ substrates. On the 3,5-dimethoxyphenyl-terminated $p\text{-Si}$ surface, MoS_x forms a continuous film across the surface, whereas the phenyl-terminated $p\text{-Si}$ surface results in fewer nucleation sites, evidenced by the spacing and varying sizes of the particles. The enhanced MoS_x deposition on the 3,5-dimethoxyphenyl-

terminated substrates are thus due to a combination of beneficial properties – primarily the higher charge density at the electrode surface due to the oxygen moieties and lower charge transfer resistance. If the potential window for the electrodeposition is expanded to the potentials used to electrodeposit films for PEC-HER tests (between -1.25 to $+0.1\text{ V}$ vs. Pt) (Figure 4e and f) then MoS_x appears to form a densely-packed nanoparticle film over the entire surface of the $p\text{-Si}(111)|\text{R}$ electrode, regardless of the identity of R. Figure S8a and b in the supplementary information show atomic force microscopy images of the $p\text{-Si}(111)|\text{diOMe}|\text{MoS}_x$ and $p\text{-Si}(111)|\text{Ph}|\text{MoS}_x$, respectively. From these images the root mean square roughness was determined to be 10.0 nm for $p\text{-Si}(111)|\text{diOMe}|\text{MoS}_x$ versus 7.4 nm for $p\text{-Si}(111)|\text{Ph}|\text{MoS}_x$, which resulted in roughness factors of 1.010 and 1.005, respectively. In addition, the thicknesses of the MoS_x films were found via AFM to be 59 nm and 29 nm for $p\text{-Si}(111)|\text{diOMe}$ and $p\text{-Si}(111)|\text{Ph}$, respectively. This difference in thickness of the films is likely attributable to the favourable qualities of the -diOMe surface functionalization.

HER Catalytic Performance

Table 2: Photoelectrocatalytic hydrogen evolution figures of merit for $p\text{-Si}(111)$ surfaces

Surfaces	V_{onset} (V)	$V_{J_{\text{max}}}$ (V)	$\Delta V (V_{\text{onset}} - V_{J_{\text{max}}})$ (V)
$p\text{-Si}(111) \text{diOMe}$	-0.24	-0.61	0.37
$p\text{-Si}(111) \text{Ph}$	-0.29	-0.80	0.51
$p\text{-Si}(111) \text{diOMe} \text{MoS}_x$	+0.14	-0.22	0.36
$p\text{-Si}(111) \text{Ph} \text{MoS}_x$	+0.05	-0.33	0.38

The activities of the MoS_x catalyst on $p\text{-Si}(111)|\text{R}$ photoelectrodes were tested for HER performance in $0.5\text{ M H}_2\text{SO}_4(\text{aq})$ under 1-sun illumination. Figure 5a shows the linear sweep voltammograms *with* and *without* the MoS_x catalyst deposited on the organic functionalized $p\text{-Si}(111)$ photoelectrodes. As shown in Figure 5a, the bare $p\text{-Si}(111)|\text{diOMe}$ photoelectrode shows an onset potential of -0.24 V vs. RHE (V_{onset} , potential at $J = -1\text{ mA cm}^{-2}$), which is more positive than bare $p\text{-Si}(111)|\text{Ph}$ photoelectrode (-0.29 V vs. RHE). Furthermore, $\Delta V (V_{\text{onset}} - V_{J_{\text{max}}})$ of $p\text{-Si}(111)|\text{diOMe}$ photoelectrode (373 mV) was significantly smaller compared to $p\text{-Si}(111)|\text{Ph}$ photoelectrode (512 mV), indicating a sharper turn-on to maximum performance. These results agree with our previous results,¹² which showed band edge modulation of $p\text{-Si}(111)$ modified with various organic functional groups. The diminished ΔV is attributed to a lower resistance to charge transfer across the electrode|electrolyte interface. In the same way, the lower ΔV of $p\text{-Si}(111)|\text{diOMe}$ can be attributed to the greater interaction of the lone pair electrons of the methoxy group with the electrolyte, as opposed to the phenyl case. After introduction of the MoS_x catalyst, the onset potential of diOMe-terminated substrate was positively shifted to $+0.14\text{ V}$ vs. RHE; higher than the $+0.05\text{ V}_{\text{onset}}$ exhibited by the Ph-terminated substrate. This difference is likely due to the band bending caused by the established surface dipole effect caused

by the introduction of organic linkers onto the surface of the *p*-Si(111) electrodes.^{11,12,45,46} In this work, it was reported that the greatest extent of band bending occurred on the *p*-Si(111)|H electrodes as compared with other surface moieties.

To demonstrate the need for organic functionalization of the Si(111) substrate, MoS_x was electrodeposited on a *p*-Si(111)|H surface (prepared by fresh HF etch) and tested for the PEC-HER (Figure S9). On the first scan the onset potential for the H-terminated surface was +0.195 V vs. RHE, more positive than the diMeO-terminated surface, indicating that the surface functionalization plays a crucial role in the photoelectrocatalytic ability of the electrode system. The *p*-Si(111)|H|MoS_x system quickly degrades, and by the 6th scan the onset potential has shifted to +0.05 V vs. RHE, continuing to decrease with each additional scan. This is due to the inability of the susceptible Si-H bonds to protect the surface from hydrolysis and oxidation. To examine the turn-on to maximum performance in the stable diOMe and Ph electrodes, the *J*-*V* curves were converted to Tafel plots as shown in Figure 5b. The *p*-Si(111)|diOMe|MoS_x film shows the smallest Tafel slope of 116 mV per decade, which is less than the Tafel slope of *p*-Si(111)|Ph|MoS_x (149 mV per decade).

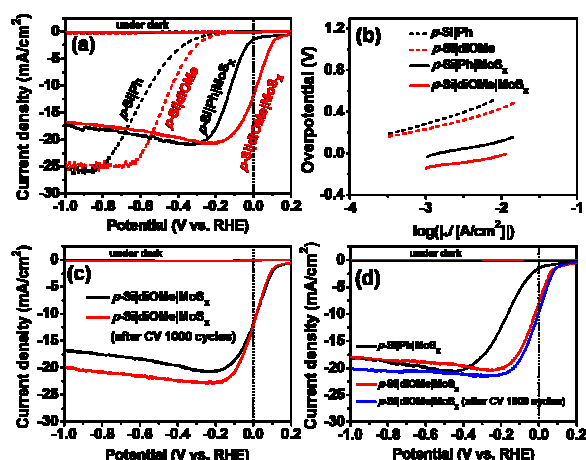


Figure 5: (a) *J*-*E* curves for the hydrogen evolution reaction and (b) Tafel plots for organic-modified *p*-Si(111) substrates with and without MoS_x catalyst. (c) Comparison of HER activity of *p*-Si(111)|diOMe|MoS_x before and after 1000 CV cycles. (d) Control: Electrodeposited MoS_x in the absence of a platinum counter-electrode, as well as PEC-tested in the absence of a platinum counter-electrode.

The stabilities of the films were tested by performing 1000 cycles on the electrode and comparing the 1000th cycle to the 1st. The stability test is shown in Figure 5c, which shows that the maximum current (*J*_{max}) increased, while *V*_{onset} remained constant. The enhancement in *J*_{max} can be explained by two processes: (i) reaction (3) and (ii) the corrosion reaction discussed in the spectroelectrochemical results of MoS_x deposition. Vruble et al. observed that upon cycling amorphous MoS₃ is converted to MoS_{2+x} (close to MoS₂), which is believed to be the stable, active form of the catalyst.²⁸ This conversion likely occurs through reaction (3). The corrosion reaction serves to remove elemental sulfur produced from reaction (2) and (3) from the electrode. Sulfur is known to

block active sites and/or decrease conductivity, both of which are deleterious to catalytic activity. The corrosion reaction also removes some of the deposited MoS_x catalyst, which could result in a higher surface area and allow more light to reach the silicon substrate. Lastly, due to the well-known complex, [Pt(MoS₄)₂]²⁻,⁴⁷ we unambiguously excluded any beneficial effect Pt (from the electrochemical apparatus) could have on both the electrodeposition and HER activity. Such control experiments were performed by exchanging the Pt counter electrode for a graphite rod or glassy carbon electrode for the electrodeposition and PEC-HER test, respectively. Figure 5d shows the resulting *J*-*V* curves, wherein the *V*_{onset} of Pt-free *p*-Si(111)|Ph|MoS_x and *p*-Si(111)|diOMe|MoS_x were +0.040 V and +0.125 V vs. RHE, respectively; these values are nearly identical to the original results found of Figure 5a.

Conclusions

The synergistic utility of coupling an ionic liquid-based, photo-assisted electrodeposition of MoS_x with organic-functionalized silicon photocathodes for HER has been demonstrated. The lone pair electrons of the 3,5-dimethoxyphenyl surface linker promoted favourable interaction across the electrode|electrolyte interface, resulting in an increase in conductivity. This linker provides enhanced physico-chemical properties for photo-assisted electrodeposition of MoS_x on *p*-Si(111) substrates. The electrodeposition of high-quality MoS_x in ionic liquid avoids issues associated with aqueous depositions, and it is proton-dependent. PEC-HER studies demonstrate that a hydrophilic surface linker on Si(111) – namely, 3,5-dimethoxyphenyl – beneficially modulates the band edge and facilitates the deposition of a continuous MoS_x film. Ultimately, this affords a device with 0.33% efficiency for solar hydrogen production.

Experimental

Preparation of Organic-Modified *p*-Si(111) Substrate

An organic-functionalized *p*-Si(111) wafer was prepared by a method analogous to our previous report.¹² A boron doped, Cz grown *p*-Si(111) wafer (single-side-polished, 450 ± 25 μm thick, Virginia Semiconductor Inc.) with 1.4-9 Ω-cm resistivity was used for organic functionalization of the surface. The *p*-Si(111) wafer washed with acetone, ethanol, and water with sonication for 10 min in each solvent. The substrate was immersed in a Piranha solution, prepared by 3:1 volume mixture of H₂SO₄ (96.6%, Fisher Scientific) and H₂O₂ (30%, Fisher Scientific), at 90 °C for 20 min. In the following step, the Si wafer was etched in a HF(aq) solution (semiconductor grade, Transene Company, Inc.) for 20 s at room temperature. The atomically flat H-terminated Si(111) surface was then generated by immersing the wafer in a degassed NH₄F(aq) solution (semiconductor grade, Transene Company, Inc.) for 20 min. After washing with deionized water and drying under a stream of N₂ gas, it was transferred to a glove box under inert atmosphere (N₂). The H-terminated silicon surface was

chlorinated PCl_5 (99.998%, Alfa Aesar) in saturated chlorobenzene (99.8%, Sigma-Aldrich) at 90 °C for 45 min. In order to initiate the chlorination, a grain of benzoyl peroxide (reagent grade, 97%, Sigma-Aldrich) was added to the PCl_5 /chlorobenzene solution. After serial washing with chlorobenzene and tetrahydrofuran (THF), the wafer was reacted with the desired lithiated organic compound for attachment of phenyl or 3,5-dimethoxyphenyl. For the phenyl-terminated Si(111) surface (p -Si(111)|Ph), the Cl-terminated Si(111) wafer was immersed in 0.1 M phenyllithium (PhLi) solution in THF (diluted from 1.8 M PhLi in dibutyl ether, Sigma-Aldrich) at -70 °C, then the solution was allowed to warm to room temperature and stored for 1 h. Because the atop Si atoms cannot be fully covered with the aryl groups, the unreacted Si(111)-Cl sites were methylated using 1 M CH_3MgCl solution (diluted from 3.0 M in THF, Sigma-Aldrich) at 60 °C for 30 min. The wafer was removed from solution, rinsed with THF, sonicated in THF and MeOH for 10 min, dried by a stream of N_2 gas, and finally dried under vacuum. For the 3,5-dimethoxyphenyl-terminated Si(111) surface (p -Si(111)|diOMe), a small batch of 0.082 g (0.36 mmol) of 1-bromo-3,5-dimethoxybenzene (97%, Acros) was reacted with 0.2 mL of n -butyllithium ($n\text{BuLi}$) solution (0.32 mmol, 1.6 M in hexanes, Sigma-Aldrich) in 15 mL THF at -70 °C for 40 min. The Cl-terminated Si(111) wafer was immersed into the lithiated dimethoxybenzene solution at -70 °C, then the solution was allowed to warm to room temperature and stored for 1 h. The unreacted Si(111)-Cl sites were alkylated with methyl groups analogous to the phenyl-terminated Si(111).

Photo-Assisted Electrodeposition of MoS_x

Synthesis of $[\text{MePipH}]_2[\text{MoS}_4]$. $[\text{MePipH}]_2[\text{MoS}_4]$ was synthesized by a modification of a published procedure.^{48,49} $[\text{NH}_4]_2[\text{MoS}_4]$ (7.71 mmol, 99.97%, Sigma-Aldrich) was added to 115 mL distilled H_2O , followed by the addition of N -methylpiperidine (15.4 mmol, 99%, Sigma-Aldrich). The solution was stirred for 1 hour under an N_2 atmosphere. The reaction was exposed to slight vacuum for 1 min every 5 min for 1 h to remove NH_3 . The solution was then filtered, and a volume of 115 mL of ethanol was added to the filtrate, and it was placed in a freezer overnight. The resulting product was collected by filtration (cold), and washed with cold ethanol (ACS grade, Pharmco-Aaper) and diethyl ether (Fisher Scientific). The product consisted of metallic, bright red flakes. Yield: 35%. UV/vis (CH_3CN , λ in nm): 244, 320, 470.

Synthesis of $[\text{PipH}][\text{TFSI}]$. $[\text{PipH}][\text{TFSI}]$ was synthesized by a modification of a published procedure.⁵⁰ Piperidine (8.997 mmol, 99%, Sigma-Aldrich) was dissolved in 5.0 mL of distilled H_2O , placed under an N_2 atmosphere, and cooled to ca. 0 °C in an ice bath. Excess of 80 wt% HTFSI(aq) (16.582 mmol, 99%, IoLiTec, Inc.) was diluted with 5 mL of distilled H_2O and added dropwise to the solution over 30 min. The reaction was allowed to warm to room temperature and was left stirring overnight. The product was transferred to a separatory funnel, extracted into 50 mL of CH_2Cl_2 (ACS grade, Fisher Scientific),

and washed three times with 50 mL of CH_2Cl_2 . The CH_2Cl_2 was then removed with a rotary evaporator. The product was dried under vacuum at 50 °C for at least 24 h. The product was a clear liquid. Yield 76%.

Photo-Assisted Electrodeposition of MoS_x and Spectroelectrochemistry of $[\text{MePipH}]_2[\text{MoS}_4]$.

The photo-assisted electrodeposition experiments were performed on a CH instruments 440 potentiostat/galvanostat with a homemade glass cup three electrode cell. All experiments were performed using 1-ethyl-3-methylimidazolium bis(trifluoromethylsulfonyl)imide (EMIM-TFSI, 99%, IoLiTec, Inc.). EMIM-TFSI was dried in a vacuum oven at 100 °C for a minimum of 24 h prior to use and stored in an argon-filled glovebox. A Cree 100 W white LED bulb (color temperature = 2,700 K) in an aluminum cone was used as the light source. Prior to experiments, the cell was soaked in a Piranha solution for 24 h, followed by neutralization with NaHCO_3 , boiling in distilled H_2O for 1 h, and drying in an oven at 100 °C overnight. All electrodeposition experiments were performed in a glovebox with an argon atmosphere with an O_2 concentration < 5 ppm and a H_2O concentration < 0.1 ppm. The p -Si(111) substrate functionalized with the appropriate organic group was used as the working electrode. Alternatively, glassy carbon (GC, Alfa Aesar) slabs were employed as the working electrode for additional characterization of the films; these electrodes were polished with 0.050 μm alumina slurry on microcloth (Buehler), sonicated in 18.2 $\text{M}\Omega\text{-cm}$ H_2O to remove the residual alumina powder, and dried in an oven at ca. 100 °C for 24 h prior to experiments. The counter electrode in these experiments was a Pt mesh or a graphite rod; graphite was used to avoid the possibility of platinum contaminating the working electrode. The quasi-reference electrode (QRE) was a platinum wire. The electrodes were placed directly in the deposition bath. Platinum was used as the QRE as an alternative to silver, which has been observed to dissolve in ionic liquids and contaminate electrodes. It should be noted that drift in the potential up to 200 mV in platinum QREs have been observed. The potential in reference to ferrocene could not be determined due to a reaction between ferrocene and the MoS_4^{2-} precursor. The reaction between M^{2+} ions and MoS_4^{2-} has been known to lead to various soluble and insoluble products.⁴⁷ Before use the platinum counter and quasi-reference electrode were cleaned by heating in a propane flame, graphite rods were polished with sand paper. After the deposition experiments the working electrode was removed from the glovebox and subsequently washed with ethanol, acetone (ACS grade, Fisher Scientific), and dichloromethane to remove any residual ionic liquid.

UV/vis spectroelectrochemical measurements were performed in a homemade, air-tight Kel-F three electrode cell with a 1 cm path length. Prior to use the cell was soaked in a Piranha solution for 24 h followed by neutralization with NaHCO_3 , boiling in H_2O for 1 h, and dried under vacuum at ca. 100 °C overnight. The cell was assembled outside the glovebox, brought into the glovebox to add the electrolyte; the cell was sealed and removed from the glovebox to perform

experiments. The working electrode was transparent fluorine-doped tin oxide (FTO, Pilkington). The FTO electrodes were cleaned by sequential sonication in acetone, ethanol, and isopropanol for 10 min, heating in 30 v/v% aqueous ethanolamine solution at 80 °C for 10 min, sonication in water for 30 min, drying under N₂ and in an oven at ca. 100 °C overnight. The counter-electrode and quasi-reference electrode were a stainless steel rod and a Pt wire, respectively. The stainless steel electrode was cleaned with sand paper and the Pt wire was cleaned by heating in a propane flame. These electrodes are placed directly in the solution. A diode array UV/vis spectrometer (Agilent 8453) was used to measure several wavelengths during the experiment. Due to noise in the UV/vis spectrum, it was not possible to record absorption data for wavelengths below 380 nm and between 410–550 nm. During spectroelectrochemical measurements, the shutter remained open to collect measurements at a rate of one per second.

Physical and Electrochemical Characterization of Electrodeposited Films

Hydrophilicity was determined by using a water contact angle measurement of the organic-modified Si(111) samples using a contact angle goniometer (Model 100-00-115, Rame Hart), and by measuring the contact angle values of a 10 µL water droplet. The electrodeposited films were characterized using several techniques. Scanning electron microscopy was performed on a FEI Quanta 650 FEG ESEM. Films were coated with a thin layer of Au/Pd to ensure conductivity of the films. Raman spectroscopy was carried out on a Renishaw inVia microscope with a 514.5 nm Ar laser in the backscattering configuration. The Stoke's Raman signal at 521 cm⁻¹ of a bulk Si(110) single crystal was used to calibrate the instrument. The laser was operated at low powers (1%, < 0.5 mW) to prevent photocrystallization or degradation of the MoS_x films. X-ray photoelectron spectra were collected on a Kratos Axis Ultra DLD X-ray photoelectron spectroscopy system and analysed according to the same methods as our previous work.⁵¹ Survey scans were recorded with a 1 eV resolution, followed by high resolution scans (0.1 eV, 2000 ms dwell time) of the carbon 1s, oxygen 1s, molybdenum 3d, and sulfur 2p. Semi-quantitative analysis of the XPS spectra was performed with the CasaXPS software (version 2.3.16, Casa Software Ltd.). The high resolution scans were used to compare the relative concentrations of the different species comprising the film. Non-metals, C and O, were fit with linear backgrounds and Mo and S were fit with Shirley backgrounds. The O–C=O peak from adventitious carbon in the C 1s spectrum was used to calibrate the binding energy. All fitted curves were the result of the summation of multiple Voigt functions with 30% Lorentzian and 70% Gaussian character.

The photoelectrochemical (PEC) properties of surface-modified samples were investigated in a three-electrode configuration, consisting of a Si wafer working electrode, a Pt-wire (99.95%, Strem) counter electrode, and a saturated calomel electrode (CHI150, CH Instruments) as a reference

electrode. For the HER performance measurements of the MoS_x substrates (electrodeposited with a graphite rod counter electrode instead of a Pt electrode), a glassy carbon electrode (CHI104, CH Instruments) was used as a counter electrode. A 0.5 M H₂SO_{4(aq)} solution was used as the electrolyte in all PEC-HER measurements. A 150 W Xe lamp (Newport Co.) with an AM-1.5G solar filter (Newport Co.) was used to simulate sunlight at 100 mW cm⁻². The light active area was defined as 0.07 cm² from the diameter of the O-ring (0.3 cm), and the photocurrent density (mA cm⁻²) was converted based on the light active area. The detailed experimental set-up, including PEC-cell assembly is available in our previous report. The linear sweep voltammetry (LSV) was performed using a WaveNow (Pine Research Instrumentation) potentiostat between +0.2 V and -1.3 V vs. SCE with a standard scan rate of 100 mV s⁻¹. To convert the measured potential (vs. SCE) to RHE, the following equation was used:

$$E_{RHE} = 0.241 V + 0.059pH \quad (4)$$

Electrochemical impedance spectroscopy (EIS) measurements were carried out using an Interface 1000 (Gamry Instruments) at various applied potentials between 0 V and -0.4 V vs. SCE under illumination with an AC amplitude of 10 mV over a frequency range of 10⁵–0.1 Hz. For the extraction of charge transfer resistance (*R_{ct}*) from the EIS results, the Randles equivalent circuit was applied using Zview software (version 2.8d, Scribner Associate Inc.).

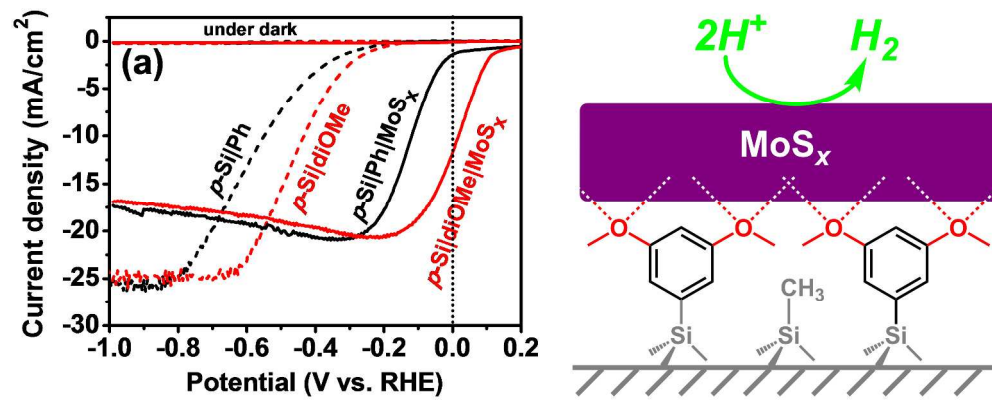
Acknowledgements

Financial support for this work was provided by the R.A. Welch Foundation (grant F-1529, DWR and KJS). Support for HJK and MJR was provided by the Office of Naval Research (N00014-13-1-0530), Welch Foundation (F-1822) and the ACS-Petroleum Research Fund (53542-DN13). DWR thanks Will Hardin and Caleb Alexander for assistance with XPS measurements and Dylan Boucher for assistance with EIS and PEC measurements. The Kratos XPS was funded by the National Science Foundation under grant CHE-0618242.

References

- (1) Oh, I.; Kye, J.; Hwang, S. *Nano Lett.* **2011**, *12*, 298–302.
- (2) Goodey, A. P.; Eichfeld, S. M.; Lew, K.-K.; Redwing, J. M.; Mallouk, T. E. *J. Am. Chem. Soc.* **2007**, *129*, 12344–12345.
- (3) Boettcher, S. W.; Warren, E. L.; Putnam, M. C.; Santori, E. A.; Turner-Evans, D.; Kelzenberg, M. D.; Walter, M. G.; McKone, J. R.; Brunschwig, B. S.; Atwater, H. A.; Lewis, N. S. *J. Am. Chem. Soc.* **2011**, *133*, 1216–1219.
- (4) Dai, P.; Xie, J.; Mayer, M. T.; Yang, X.; Zhan, J.; Wang, D. *Angew. Chem. Int. Ed.* **2013**, *52*, 11119–11123.
- (5) Choi, M. J.; Jung, J.-Y.; Park, M.-J.; Song, J.-W.; Lee, J.-H.; Bang, J. H. *J. Mater. Chem.* **2014**, *2*, 2928–2933.
- (6) Seger, B.; Pedersen, T.; Laursen, A. B.; Vesborg, P. C. K.; Hansen, O.; Chorkendorff, I. *J. Am. Chem. Soc.* **2013**, *135*, 1057–1064.

- (7) Dasgupta, N. P.; Liu, C.; Andrews, S.; Prinz, F. B.; Yang, P. J. *Am. Chem. Soc.* **2013**, *135*, 12932–12935.
- (8) McKone, J. R.; Warren, E. L.; Bierman, M. J.; Boettcher, S. W.; Brunschwig, B. S.; Lewis, N. S.; Gray, H. B. *Energy & Environ. Sci.* **2011**, *4*, 3573–3583.
- (9) Warren, E. L.; McKone, J. R.; Atwater, H. A.; Gray, H. B.; Lewis, N. S. *Energy & Environ. Sci.* **2012**, *5*, 9653–9661.
- (10) Kye, J.; Shin, M.; Lim, B.; Jang, J.-W.; Oh, I.; Hwang, S. *ACS Nano* **2013**, *7*, 6017–6023.
- (11) Grimm, R. L.; Bierman, M. J.; O’Leary, L. E.; Strandwitz, N. C.; Brunschwig, B. S.; Lewis, N. S. *J. Phys. Chem. C* **2012**, *116*, 23569–23576.
- (12) Seo, J.; Kim, H. J.; Pekarek, R. T.; Rose, M. J. *J. Am. Chem. Soc.* **2015**, *137*, 3173–3176.
- (13) Nemanick, E. J.; Hurlley, P. T.; Brunschwig, B. S.; Lewis, N. S. *J. Phys. Chem. B* **2006**, *110*, 14800–14808.
- (14) Webb, L. J.; Lewis, N. S. *J. Phys. Chem. B* **2003**, *107*, 5404–5412.
- (15) Hunger, R.; Jaegermann, W.; Merson, A.; Shapira, Y.; Pettenkofer, C.; Rappich, J. *J. Phys. Chem. B* **2006**, *110*, 15432–15441.
- (16) He, T.; Ding, H.; Peor, N.; Lu, M.; Corley, D. A.; Chen, B.; Ofir, Y.; Gao, Y.; Yitzchaik, S.; Tour, J. M. *J. Am. Chem. Soc.* **2008**, *130*, 1699–1710.
- (17) Laursen, A. B.; Pedersen, T.; Malacrida, P.; Seger, B.; Hansen, O.; Vesborg, P. C. K.; Chorkendorff, I. *J. Phys. Chem. Chem. Phys.* **2013**, *15*, 20000–20004.
- (18) Seger, B.; Laursen, A. B.; Vesborg, P. C. K.; Pedersen, T.; Hansen, O.; Dahl, S.; Chorkendorff, I. *Angew. Chem.* **2012**, *51*, 9128–9131.
- (19) Hou, Y.; Abrams, B. L.; Vesborg, P. C. K.; Björketun, M. E.; Herbst, K.; Bech, L.; Setti, A. M.; Damsgaard, C. D.; Pedersen, T.; Hansen, O.; Rossmeyl, J.; Dahl, S.; Nørskov, J. K.; Chorkendorff, I. *Nat. Mater.* **2011**, *10*, 434–438.
- (20) Tran, P. D.; Pramana, S. S.; Kale, V. S.; Nguyen, M.; Chiam, S. Y.; Batabyal, S. K.; Wong, L. H.; Barber, J.; Loo, J. *Chem. Eur. J.* **2012**, *18*, 13994–13999.
- (21) Zhang, L.; Liu, C.; Wong, A.; Resasco, J.; Yang, P. *Nano Res.* **2015**, *8*, 281–287.
- (22) Ding, Q.; Meng, F.; English, C. R.; Cabañ-Acevedo, M.; Shearer, M. J.; Liang, D.; Daniel, A. S.; Hamers, R. J.; Jin, S. *J. Am. Chem. Soc.* **2014**, *136*, 8504–8507.
- (23) Zhang, X.; Meng, F.; Mao, S.; Ding, Q.; Shearer, M. J.; Faber, M. S.; Chen, J.; Hamers, R. J.; Jin, S. *Energy & Environ. Sci.* **2015**, *8*, 862–868.
- (24) Ding, Q.; Zhai, J.; Cabán-Acevedo, M.; Shearer, M. J.; Li, L.; Chang, H.-C.; Tsai, M.-L.; Ma, D.; Zhang, X.; Hamers, R. J. *Adv. Mater.* **2015**, *27*, 6511–6518.
- (25) Bélanger, D.; Laperrière, G.; Marsan, B. *J. Electroanal. Chem.* **1993**, *347*, 165–183.
- (26) Ponomarev, E. A.; Neumann-Spallart, M.; Hodes, G.; Levy-Clement, C. *Thin Solid Films* **1996**, *280*, 86–89.
- (27) Merki, D.; Fierro, S.; Vrubel, H.; Hu, X. *Chem. Sci.* **2011**, *2*, 1262–1267.
- (28) Vrubel, H.; Hu, X. *ACS Catal.* **2013**, *3*, 2002–2011.
- (29) Ponomarev, E. A.; Albu-Yaron, A.; Tenne, R.; Lévy-Clement, C. *J. Electrochem. Soc.* **1997**, *144*, L277–L279.
- (30) Albu-Yaron, A.; Levy-Clement, C.; Hutchison, J. L. *Electrochem. Solid-state Lett.* **1999**, *2*, 627–630.
- (31) Endres, F.; MacFarlane, D.; Abbott, A. *Electrodeposition from ionic liquids*; John Wiley & Sons, 2008.
- (32) Murugesan, S.; Kearns, P.; Stevenson, K. J. *Langmuir* **2012**, *28*, 5513–5517.
- (33) Murugesan, S.; Akkineni, A.; Chou, B. P.; Glaz, M. S.; Vanden Bout, D. A.; Stevenson, K. J. *ACS nano* **2013**, *7*, 8199–8205.
- (34) Kawamura, Y. L.; Sakka, T.; Ogata, Y. H. *Electrochemistry* **2008**, *76*, 121–124.
- (35) Kawamura, Y. L.; Sakka, T.; Ogata, Y. H. *J. Electrochem. Soc.* **2005**, *152*, C701–C705.
- (36) Maier, C. U.; Specht, M.; Bilger, G. *Int. J. Hydrog. Energy* **1996**, *21*, 859–864.
- (37) Yoshihara, S.; Endo, K.; Sato, E.; Bockris, J. O. ’. *M. J. Electroanal. Chem.* **1994**, *372*, 91–94.
- (38) Li, F.; Basile, V. M.; Pekarek, R. T.; Rose, M. J. *ACS Appl. Mater. & Interfaces* **2014**, *6*, 20557–20568.
- (39) Kim, H. J.; Kearney, K. L.; Le, L. H.; Pekarek, R. T.; Rose, M. J. *ACS Appl. Mater. & Interfaces* **2015**, *7*, 8572–8584.
- (40) Benoist, L.; Gonbeau, D.; Pfister-Guillouzo, G.; Schmidt, E.; Meunier, G.; Levasseur, A. *Thin Solid Films* **1995**, *258*, 110–114.
- (41) Muijsers, J. C.; Weber, T.; Vanhardeveld, R. M.; Zandbergen, H. W. _.; Niemantsverdriet, J. W. *J. Catal.* **1995**, *157*, 698–705.
- (42) Weber, T.; Muijsers, J. C.; Niemantsverdriet, J. W. *J. Phys. Chem.* **1995**, *99*, 9194–9200.
- (43) Liang, K. S.; Cramer, S. P.; Johnston, D. C.; Chang, C. H.; Jacobson, A. J.; Chianelli, R. R. *J. Non-Crystalline Solids* **1980**, *42*, 345–356.
- (44) Chang, C. H.; Chan, S. S. *J. Catal.* **1981**, *72*, 139–148.
- (45) Gleason-Rohrer, D. C.; Brunschwig, B. S.; Lewis, N. S. *J. Phys. Chem. C* **2013**, *117*, 18031–18042.
- (46) Hiremath, R. K.; Rabinal, M. K.; Mulimani, B. G.; Khazi, I. M. *Langmuir* **2008**, *24*, 11300–11306.
- (47) Müller, A.; Diemann, E.; Jostes, R.; Bögge, H. *Angew. Chem. Int. Ed. Engl.* **1981**, *20*, 934–955.
- (48) Srinivasan, B. R.; Dhuri, S. N.; Poisot, M.; Näther, C.; Bensch, W. *Z. für Naturforsch. B* **2004**, *59*, 1083–1092.
- (49) Siemeling, U.; Bretthauer, F.; Bruhn, C. *Z. für Anorg. und Allg. Chem.* **2006**, *632*, 1027–1032.
- (50) Fericola, A.; Panero, S.; Scrosati, B.; Tamada, M.; Ohno, H. *ChemPhysChem* **2007**, *8*, 1103–1107.
- (51) Redman, D. W.; Murugesan, S.; Stevenson, K. J. *Langmuir* **2013**, *30*, 418–425.



294x117mm (300 x 300 DPI)